RSC Advances

PAPER

View Article Online
View Journal | View Issue

Cite this: *RSC Adv.*, 2025, **15**, 29879

Influence of hydrogen bonding on twisted intramolecular charge transfer in coumarin dyes: an integrated experimental and theoretical investigation

Jing Ge, Jing Xiao, Bingqian Xue, Duidui Liu, Bingqi Du and Xilin Bai *

Twisted intramolecular charge transfer (TICT) is a critical mechanism influencing the emission efficiency and stability of fluorescent materials, thereby playing a pivotal role in the design of highly fluorescent and stable dyes. Although substantial research has concentrated on the role of intermolecular hydrogen bonding in excited-state dynamics, the impact of intramolecular hydrogen bonding has not been thoroughly investigated. To elucidate the solvent polarity dependence of C7 and C30, we employed the Kamlet–Taft and Catalán 4P models in conjunction with steady-state and transient absorption spectroscopy, complemented by time-dependent density functional theory (TDDFT) calculations. Our findings demonstrate that C30 exhibits a pronounced TICT process in both solvents. Conversely, C7, stabilized by intramolecular hydrogen bonds, retains a planar configuration of its benzimidazole and benzopyrone moieties, effectively preventing the TICT process. Moreover, in MeOH, the intermolecular hydrogen bonding in C30 significantly extends the lifetime of the TICT state compared to ACN. Theoretical analyses of electrostatic potential, molecular geometry, and frontier molecular orbitals further corroborate these observations. This work provides valuable insights into the design of fluorescent dye molecules and the selection of solvents, laying a foundation for advancing the photophysical and photochemical understanding of coumarin dyes.

Received 16th April 2025
Accepted 7th August 2025

DOI: 10.1039/d5ra02669e

rsc.li/rsc-advances

Introduction

Fluorescent dyes are rapidly transitioning from a trial-and-error approach to a molecular engineering strategy. Increasing evidence suggests that twisted intramolecular charge transfer (TICT) has emerged as a key mechanism for achieving the design of highly fluorescent and stable dyes.[1–9] The TICT process is characterized by charge transfer (CT) between donor and acceptor groups within a molecule upon photoexcitation, accompanied by molecular twisting. Understanding of this process is vital for elucidating the photophysical behavior of dye molecules. The TICT model, initially proposed by Grabowski *et al.*, accounts for the dual fluorescence phenomenon, attributing high fluorescence to intramolecular charge transfer (ICT) and low fluorescence to the TICT state, as observed in DMABN molecules.[10] Since its inception, this model has been instrumental in exploring TICT behavior across various fluorescent materials, enabling significant improvements in emission efficiency by controlling the transition from non-emissive to emissive states. These advancements have expanded the application of fluorescent materials in fields such as bioimaging, sensors, and fluorescent probes.[11–19] Recent studies have shown the substantial impact of hydrogen bonding on intramolecular charge distribution in fluorescent molecules, which directly influences their fluorescent properties and the formation of TICT states.[20–28] Hydrogen bonds can alter the excited-state structure of molecules, thereby affecting the formation of ICT or TICT states. Therefore, understanding the influence of hydrogen bonding on the TICT process is crucial for designing efficient fluorescent materials.

Coumarins and their derivatives, particularly the 7-amino-substituted variants, represent a significant class of benzopyranone-based organic fluorescent dyes with widespread research interest.[29,30] These dyes exhibit unique fluorescent properties under various conditions, making them valuable in studying photophysical processes. Their fluorescence is highly sensitive to solvent polarity, viscosity, and temperature, allowing them to serve as fluorescent probes for monitoring subtle changes in chemical and biological processes. Notably, these dyes demonstrate pronounced solvent-polarity-dependent Stokes shifts upon photoexcitation, with Kamlet–Taft (K–T) solvent parameters (π^*, α, β) providing further insights into the role of hydrogen bonding on the excited-state dynamics of coumarin dyes.[31] Further research indicates that 7-amino-substituted coumarin derivatives exhibit higher dipole

School of Physics and Information Engineering, Shanxi Normal University, Taiyuan 030031, China. E-mail: bxl5630@mail.ustc.edu.cn

moments, red-shifted spectra, and enhanced quantum yields in polar solvents, highlighting their potential as fluorescent probes.[32,33] For instance, Chudoba *et al.* employed femtosecond vibrational spectroscopy to study the excited-state dynamics of hydrogen-bonded complexes of coumarin 102 in trichloromethane and phenol, revealing a significant enhancement of hydrogen bonding upon photoexcitation.[34] In 2004, Senthilkumar *et al.* discovered that the TICT state of coumarin 30 (C30) exclusively exists in highly polar protic solvents, a phenomenon closely linked to intermolecular hydrogen bonding.[35] Further, in 2009, Satpati *et al.* elucidated the crucial role of protic solvents in facilitating the formation of the TICT state in coumarin 7 (C7) dyes through studies in various protic solvents and solvent mixtures.[30] Barman *et al.*, in 2013, combined time-dependent density functional theory (TDDFT) with fluorescence spectroscopy to investigate coumarin 102 hydrogen-bonded complexes, finding that hydrogen bonding promoted the excited-state ICT process.[36] Li *et al.* through TDDFT studies, further demonstrated that hydrogen bonding facilitates the formation of the TICT process in coumarin dyes such as C460.[23] Ge *et al.* conducted ultrafast excited-state dynamics studies on ICT and enhanced hydrogen bonding in the excited state for coumarin 540A and 503 across a range of solvents.[15,37] Despite extensive literature, many aspects of the photophysical properties of 7-amino coumarin dyes, particularly the influence of molecular structure on excited-state dynamics and the role of intramolecular hydrogen bonding in CT processes, remain insufficiently explored. Addressing these critical issues will not only deepen our understanding of the photophysical behavior of coumarin dyes but also provide a robust theoretical foundation for the development of novel fluorescent probes and sensors.

This study investigates the ultrafast dynamics of two structurally analogous coumarin dyes, C7 and C30 (Fig. 1), distinguished by the substitution of the NH group in the 3-benzimidazole moiety of C7 with an NCH_3 group in C30. Solvents with varying polarity and hydrogen bonding capabilities were selected to investigate the impact of hydrogen bonding on the excited-state dynamics of the molecules. Ground- and excited-state structures of the hydrogen-bonded complexes were optimized using TDDFT. Theoretical analyses, including electronic spectra, electrostatic potential (ESP), and frontier molecular orbitals, were conducted to support and interpret the experimental findings. This integrative approach elucidates the mechanism underlying the formation of TICT states, offering crucial insights into the photophysics of coumarin dyes and advancing the design of next-generation fluorescent probes and sensors.

Experimental and computational methods

Experimental

The C7 and C30 molecular samples (purity > 95.0%) were purchased from Aladdin Inc. and used without further purification. Anhydrous, spectroscopic-grade cyclohexane (Cy), tetrahydrofuran (THF), acetonitrile (ACN), methanol (MeOH), and other solvents were sourced from Macklin Inc. C7 and C30 were dissolved in these solvents, respectively, at concentrations of 80 μmol L^{-1}, which were subsequently placed in 10 mm path length quartz cuvettes. Steady-state absorption and fluorescence spectra, as well as quantum yields (QYs), were recorded using a FluoroMax+ spectrofluorometer (Horiba). TA spectra were acquired using a femtosecond pump–probe setup consisting of an Astrella femtosecond laser (Coherent), a TOPAS-Prime optical parametric amplifier (Coherent), and a Transpec FS pump–probe system (Zhongzhi Keyi). The femtosecond laser generated 800 nm pulses (1 kHz, 35 fs) that were split in a 7 : 3 ratio. The stronger pulse was used to generate 375 nm pump pulses *via* the optical parametric amplifier, while the weaker pulse formed the probe beam. The probe and pump beams were spatially overlapped at the sample position. TA spectra were collected using a spectrometer calibrated in both wavelength and intensity with a standard argon lamp, and further chirp correction was implemented to precisely determine the timing of the transient spectra. The absorbance change is given by eqn (1), where I_{probe}^{pump} and I_{probe}^{0} represent the probe signal intensities with and without the pump pulse applied to the sample, respectively. All measurements were conducted at room temperature and ambient pressure.

$$\Delta A(\lambda,t) = -\log[I_{probe}^{pump}/I_{probe}^{0}] \quad (1)$$

Computational

The geometry optimizations and electronic spectra of the hydrogen-bonded complexes of C7 and C30 in the ground state were carried out at the B3LYP/Def2-SVP level. To avoid the occurrence of artificial TICT states—often observed when scanning the excited-state potential energy surface with B3LYP—the CAM-B3LYP functional, known for its improved accuracy in describing charge-transfer excitations, was employed for excited-state calculations. Given the importance of weak intermolecular interactions, all calculations incorporated Grimme's D3 dispersion correction with Becke–Johnson damping (D3BJ). Solvent effects were accounted for using the

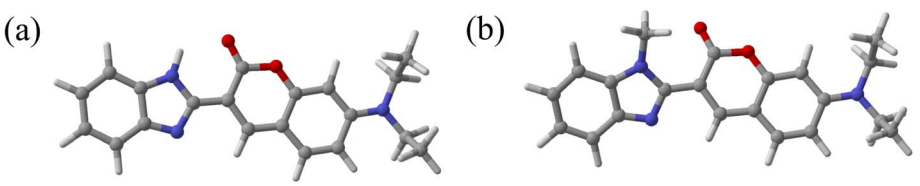

Fig. 1 Molecular structure diagram of C7 (a) and C30 (b).

SMD implicit solvent model, which provides enhanced reliability in solvation energy predictions. Harmonic vibrational frequency analyses were carried out to confirm the nature of all optimized structures. To further investigate charge distribution and electron delocalization, electrostatic potential (ESP) maps were generated based on Mulliken population analysis. Finally, frontier molecular orbitals were analyzed to elucidate their roles in the intramolecular charge-transfer.[38] All quantum chemical calculations were performed using the Gaussian 09 software package.[39]

Results and discussions

This study aims to elucidate the role of both intramolecular and intermolecular hydrogen bonding in modulating the excited-state dynamics of C7 and C30 hydrogen-bonded complexes. The solvatochromism was studied by using the Kamlet–Taft model[40,41] and the Catalán 4P model,[42] the relevant parameters are shown in Table S1.

Steady-state absorption and fluorescence spectra

The normalized steady-state absorption and fluorescence spectra of C7 and C30 in Cy, THF, AN, and MeOH are presented in Fig. 2. Specifically, C7 exhibits absorption maxima in Cy, THF, ACN and MeOH were 422 nm, 431 nm, 440 nm and 445 nm respectively, with corresponding fluorescence maxima at 459 nm, 480 nm, 490 nm, and 494 nm, respectively (Fig. 2). With the enhancement of the solvent polarity, the absorption and fluorescence peak of C7 showed a slight redshift. A similar trend is observed for C30, aligning with the findings of Satpati *et al.* TDDFT calculations were also performed to analyze the electronic excitation energies and oscillator strengths for the S_0-to-S_1 transitions of C7 and C30 in ACN and MeOH. The TDDFT results (Table 1) indicate that the oscillator strengths corresponding to the S_1 states of C7 and C30 in ACN and MeOH are the greatest, the S_1 state is derived from the transition between HOMO and LUMO, with orbital transition contributions exceeding 98%. The calculated absorption maxima for C7–ACN, C7–MeOH, C30–ACN, and C30–MeOH are 423 nm, 425 nm, 397 nm, and 404 nm, respectively. Moreover, the TDDFT calculated fluorescence emission energies and corresponding oscillator strengths for C7 and C30 in ACN and MeOH are provided in Table 2. Theoretical calculations reveal that the oscillator strength corresponding to the S_1 state of the hydrogen bond complexes C7–ACN, C7–MeOH, C30–ACN and C30–MeOH is the largest, indicating that the fluorescence maxima of these

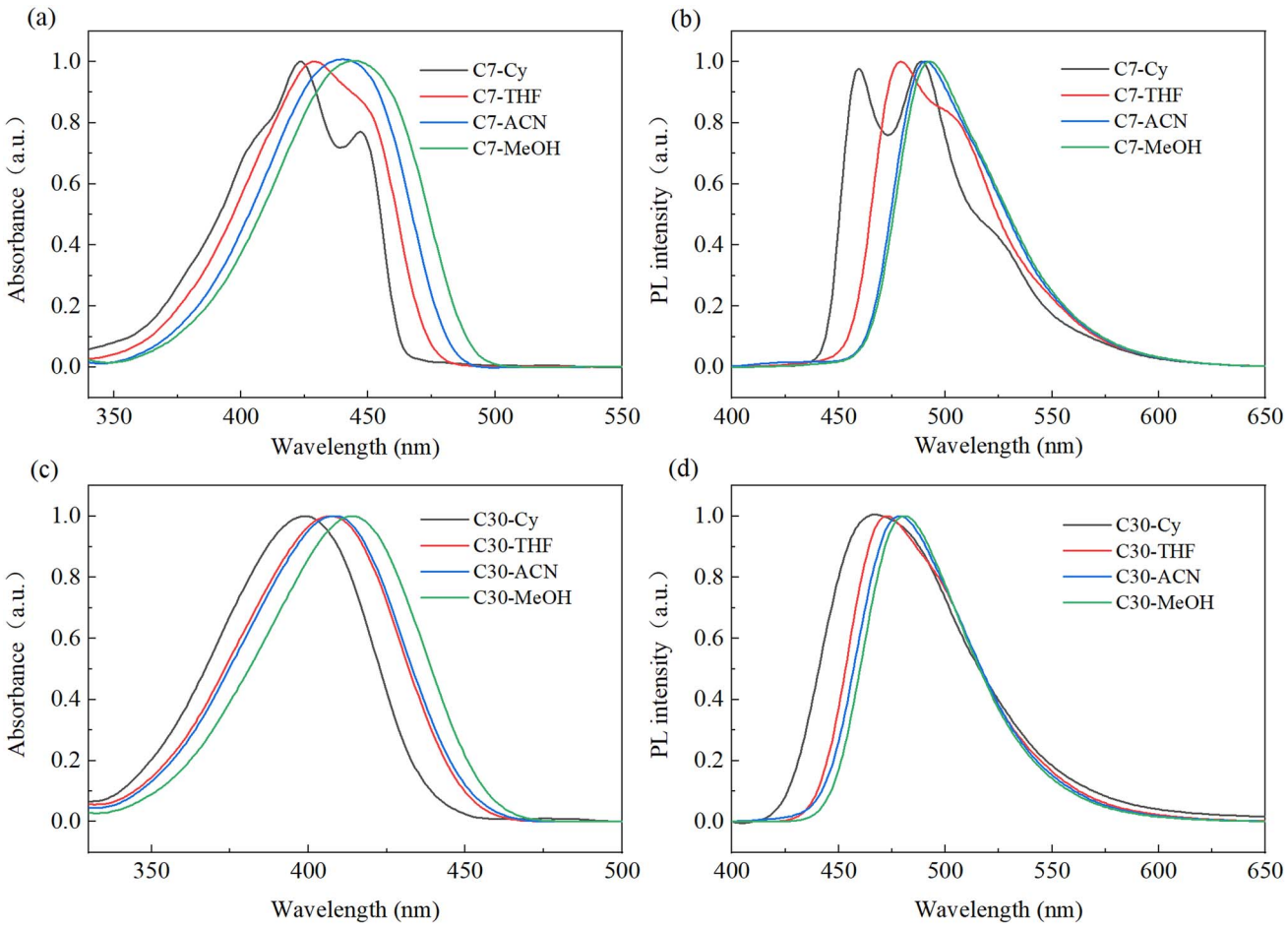

Fig. 2 Steady-state absorption (a) and (c) and fluorescence emission (b) and (d) spectra of C7/C30 in Cy, THF, ACN and MeOH (λ_{ex} = 375 nm).

Table 1 The calculated vertical excitation energies (nm) and corresponding oscillator strengths for C7 and C30 hydrogen-bonded complexes

Molecule	C7–ACN	C7–MeOH	C30–ACN	C30–MeOH
S_1	423(0.763) H → L98.9%	425(0.759) H → L98.8%	397(0.833) H → L98.2%	404(0.806) H → L98.3%
S_2	332(0.013)	332(0.009)	323(0.007)	329(0.008)
S_3	317(0.006)	318(0.005)	313(0.005)	317(0.002)
S_4	305(0.030)	306(0.056)	299(0.021)	302(0.072)
S_5	295(0.165)	297(0.164)	292(0.120)	295(0.110)
S_6	273(0.024)	292(0.003)	273(0.015)	281(0.002)

Table 2 The calculated fluorescence emission energy (nm) and corresponding oscillator strengths for C7 and C30 hydrogen-bonded complexes

Molecule	C7–ACN	C7–MeOH	C30–ACN	C30–MeOH
S_1	453(0.951)	451(0.931)	442(0.939)	444(0.915)
S_2	293(0.024)	294(0.045)	290(0.041)	292(0.063)
S_3	282(0.025)	282(0.021)	282(0.019)	281(0.021)

complexes originate from the S_1 state. The predicted emission wavelengths are 490 nm, 494 nm, 478 nm, and 481 nm, respectively, which are in close agreement with the experimentally observed fluorescence peaks summarized in Table 3. This consistency highlights the reliability of the theoretical approach in accurately capturing the excited-state dynamics of the investigated systems.

To gain deeper insight into the solvatochromic behavior of C7 and C30, we expanded the solvent set to include additional nonpolar, moderately polar, and highly polar solvents. The relevant solvent parameters are provided in the SI (Table S1). The absorption and emission maxima of C7 and C30 under different solvents were measured by a fluorescence spectrometer. As shown in Table S2, both dyes exhibit pronounced redshifts in their absorption and emission peaks as solvent polarity increases. These trends are further supported by the spectral data in Fig. 2, which illustrate the absorption and emission profiles of C7 and C30 in representative solvents (Cy, THF, ACN, and MeOH), confirming that both molecules exhibit clear solvent-induced spectral shifts consistent with solvatochromic behavior.

It is worth noting that C7 has two emission peaks in Cy and THF, while there is only one emission peak in ACN and MeOH. We speculate that the occurrence of ESIPT in C7 is highly dependent on the nature of the solvent and the competition between intra- and intermolecular hydrogen bonding. In non-polar Cy and moderately polar THF—both of which lack hydrogen bond donating capability—the fluorescence spectra of C7 display dual emission bands, consistent with emission from both the enol* (E*) and keto* (K*) tautomers. These findings are characteristic of the ESIPT process. In contrast, in hydrogen bond donating solvents such as ACN and MeOH, only a single emission band is observed, suggesting that the ESIPT channel is suppressed due to the formation of strong intermolecular hydrogen bonds between solvent and solute.[43,44]

Table 3 Absorption and emission peaks (nm) and Stokes shift (cm^{-1}) of C7 and C30 in ACN and MeOH

Sample	Solvent	Abs.	Em.	Stokes shift
C7	ACN	440	490	2319
	MeOH	445	494	2229
C30	ACN	408	478	3529
	MeOH	415	481	3306

Further support is provided by structural parameters in Table S3 and Fig. S1, the N_1–H_1 and H_1–O_1 bond lengths in the S_0 state are 1.017 Å and 2.021 Å, respectively. Upon excitation to the S_1 state, N_1–H_1 slightly elongates (1.019 Å), while H_1–O_1 shortens (1.972 Å), indicating that when the molecule is excited to the S_1 state, the hydrogen bond interaction is enhanced, which provides impetus for promoting the ESIPT process. In ACN and MeOH solvents, from S_0 to S_1 state, the intermolecular hydrogen bonds O_1–H_2 strengthen, whereas the intramolecular hydrogen bond N_1–H_1 remains nearly unchanged ($\Delta = 0.001$ Å). When the C7 monomers, C7–ACN and C7–MeOH, are excited to the S_1 state, H_1–O_1 shortens (Δ = 0.049 Å, 0.013 Å, 0.007 Å), suggesting that non-polar environments promote ESIPT by enhancing the excited-state hydrogen bonding interactions of C7.[45] To further prove that intermolecular hydrogen bonds hinder the ESIPT process, we conducted potential energy surface molecular analysis on C7–MeOH, as shown in Fig. S2. In the S_0 state, as the bond lengths of N_1–H_1 increase, the relative energy does not show a decreasing trend. When the bond length grows to 2.6 Å, the energy is the greatest. Similarly, in the S_1 state, the bond lengths of N_1–H_1 increase from 1.0 Å to 2.6 Å, and the energy shows an upward trend, indicating that the ESIPT process is effectively blocked in C7–MeOH.

Kamlet–Taft and Catalán 4P model

To systematically investigate solvent effects on the steady-state spectral properties of C7 and C30, we conducted the Kamlet–Taft analysis,[46–48] which quantitatively describes how various solvent polarity parameters affect the photophysical behavior of dyes. The dependence of the absorption and emission spectral peak frequency of a solute in a solvent can be analyzed by linear solvation energy relationship (LSER), and its general form is given by

$$v = v_0 + a\alpha + b\beta + s\pi^* \quad (2)$$

In the equation, v represents the spectral peak frequency of the solute in a given solvent, while v_0 corresponds to the peak frequency of the solute in the gas phase. π^* denotes the polarisability, α and β represent the hydrogen supply capacity and hydrogen receiving capacity of the solvent. The coefficients s, a, and b, derived from LSER analysis, indicate the relative contributions of these solvent properties to the observed spectral shifts. It can be seen from the fitting results in Table 4 that α, β and π^* all have an impact on C7 and C30.

Solvent effects in solvatochromic analysis comprise two components: specific and non-specific interactions. In recent

Table 4 Statistical best-fit parameters ($\times 10^3$ cm^{-1}) of the empirical solvatochromic model for C7/C30

	Kamlet–Taft model					Catalán 4P model					
	v_0	a	b	s	R^2	v_0	C_{SA}	C_{SB}	C_{SP}	C_{SdP}	R^2
C7 (abs.)	23.78 (±0.08)	−0.65 (±0.08)	0.16 (±0.13)	−1.18 (±0.11)	0.961	23.83 (±0.30)	−0.81 (±0.17)	0.12 (±0.16)	−0.28 (±0.41)	−0.90 (±0.13)	0.953
C7 (flu.)	21.81 (±0.05)	−0.47 (±0.05)	−0.34 (±0.08)	−1.43 (±0.06)	0.991	22.11 (±0.40)	−0.45 (±0.23)	−0.46 (±0.22)	−0.56 (±0.55)	−1.15 (±0.17)	0.943
C7 (Stokes shift)	1.97 (±0.05)	−0.15 (±0.06)	0.46 (±0.09)	0.26 (±0.08)	0.887	1.69 (±0.15)	−0.30 (±0.09)	0.55 (±0.08)	0.34 (±0.21)	0.24 (±0.07)	0.926
C30 (abs.)	25.13 (±0.14)	−0.57 (±0.15)	0.28 (±0.24)	−1.23 (±0.21)	0.866	23.19 (±0.34)	−0.89 (±0.19)	0.14 (±0.18)	−1.79 (±0.46)	−0.67 (±0.14)	0.939
C30 (flu.)	21.55 (±0.07)	−0.19 (±0.08)	−0.31 (±0.13)	−0.68 (±0.11)	0.920	22.12 (±0.19)	−0.27 (±0.11)	−0.31 (±0.10)	−0.89 (±0.26)	−0.53 (±0.08)	0.958
C30 (Stokes shift)	3.59 (±0.08)	−0.39 (±0.09)	0.59 (±0.14)	−0.55 (±0.11)	0.812	4.07 (±0.26)	−0.62 (±0.15)	0.45 (±0.14)	−0.91 (±0.36)	−0.14 (±0.11)	0.840

years, Catalán *et al.* proposed the Catalán 4P model,[42,49] in which the nonspecific solvent polarity parameter include solvent polarizability (SP) and solvent dipolarity (SdP) parameters. Each solvent parameter of this solvatochromic method is based on a pair of clear reference homogeneous solvatochromic fluorophores, and the solvent polarity parameter leads to a gradual change in adjacent polarizability through the solvatochromic method. For non-specific interactions, the model adopts a dielectric continuum approximation to describe solvent–solute interactions. According to Catalán 4P solvatochromic model

$$v = v_0 + C_{SA}SA + C_{SB}SB + C_{SP}SP + C_{SdP}SdP \quad (3)$$

The coefficients C_{SA}, C_{SB}, C_{SP} and C_{SdP} are determined through multivariate linear regression analysis of the solvatochromic data. The fitting results are shown in Table 4, compared with the K–T model, the Catalán 4P model describes the non-specific interactions more precisely and has a better goodness of fit, further demonstrating the solvent-induced coloration phenomenon of C7 and C30.

Transient absorption spectroscopy

Femtosecond transient absorption (fs-TA) spectroscopy is a powerful technique for investigating laser-induced ultrafast excited-state dynamics.[50,51] To explore the effects of structural differences between C7 and C30, as well as the influence of solvent hydrogen-donating ability (α), we measured the fs-TA spectra of C7 and C30 in ACN and MeOH. To visualize the evolution of the fs-TA spectra, 2D contour maps were generated (Fig. 3), with the horizontal axis representing the probe wavelength (375–675 nm) and the vertical axis indicating the time delay (0–3 ns). Red denotes positive signals, blue corresponds to negative signals, and the intensity of the color reflects the relative signal strength. Both C7 and C30 exhibit excited-state absorption (ESA) in the 375–450 nm range and stimulated emission (SE) in the 470–550 nm range.

The fs-TA spectra of C7 and C30 in different solvents are depicted in Fig. 4. For C7, a pronounced negative signal is detected in the 450–600 nm range during the initial 0–0.4 ps of evolution. At 0.8 ps, the wavelength of this negative signal stabilizes at 514 nm and 508 nm. Subsequently, after 100 ps, the intensity of the negative signal reaches its maximum before gradually decreasing. For C30, a similar negative signal is observed in the 460–600 nm range during the first 0–0.5 ps. The insets of panels (c) and (d) in Fig. 4 provide a clearer visualization of the temporal evolution of the TA spectra between 0.6 ps and 1.2 ps. During this interval, the negative signal peaks of C30 in ACN and MeOH shift from 490 nm and 492 nm to 498 nm and 503 nm, respectively. In contrast, no such spectral shift is observed for C7. This redshift, occurring around 200 fs, is attributed to the structural relaxation associated with the transition from the ICT state to the TICT state. This process is analogous to that reported by Mandal *et al.* in the transient absorption spectra of DMAPPIDCN molecules in ACN.[52] Moreover, theoretical calculations indicate a change in the dihedral angle of C30 in the S_1 state changes, providing further evidence

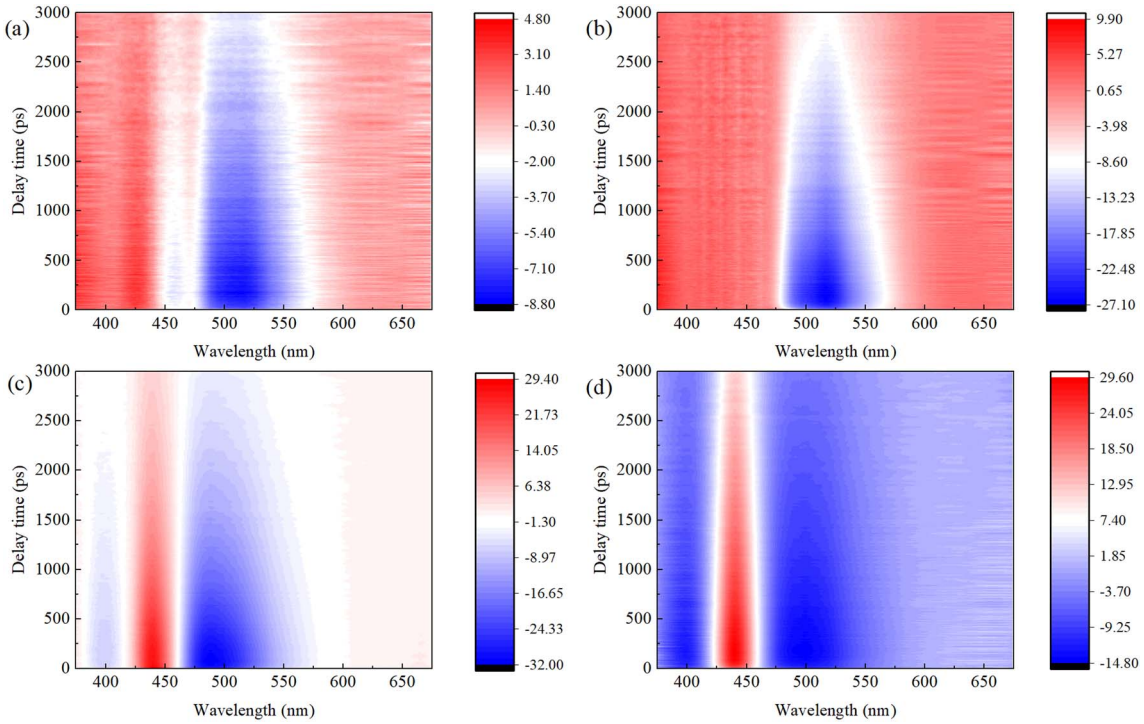

Fig. 3 2D fs-TA spectra of C7/C30 in ACN (a and c) and MeOH (b and d) (λ_{ex} = 375 nm).

for the presence of the TICT process in highly polar solvents such as ACN and MeOH.

To gain deeper insights into the excited-state decay processes of C7 and C30 in ACN and MeOH, global fitting of the fs-TA kinetics at characteristic peaks was performed. Fig. 5 displays the fs-TA kinetic curves for both molecules in various solvents, with the corresponding global fitting parameters summarized in Table 5. The decay profiles for C7 in ACN and

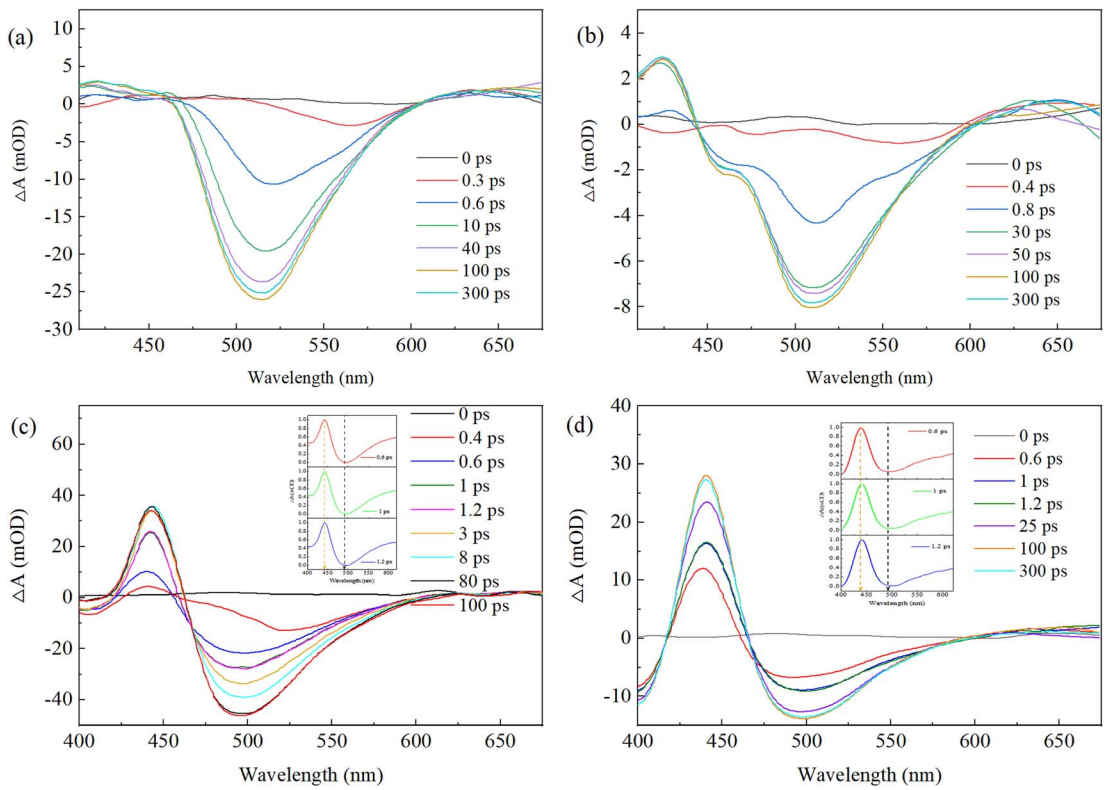

Fig. 4 Fs-TA spectra of C7/C30 in ACN (a and c) and MeOH (b and d) after excitation at 375 nm.

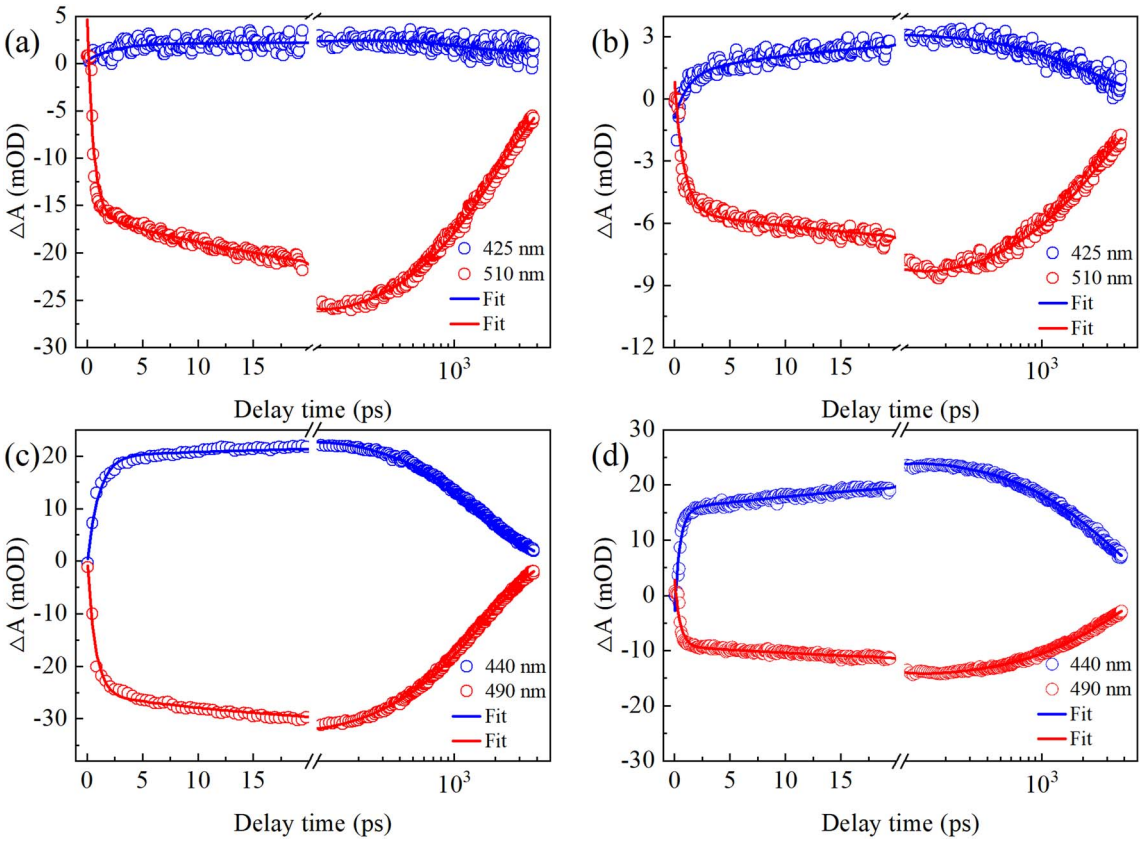

Fig. 5 TA kinetic curves of C7/C30 in ACN (a and c) and MeOH (b and d) (λ_{ex} = 375 nm).

MeOH were best fitted by a three-exponential function, whereas C30 in ACN and MeOH required a four-exponential fit, suggesting the presence of an additional relaxation process in C30's electronic excited state. Analysis of the kinetic curves at characteristic peaks reveals that the sub-100 fs time constant (τ_1) corresponds to the rapid transition from the locally excited (LE) state to the ICT state for both C7 and C30. Two slower decay components, with time constants τ_3 (tens of ps) and τ_4 (~ns), are attributed to solvent reorganization and fluorescence emission, respectively.[53,54] Additionally, C30 exhibits a fast decay component τ_2 (~11 ps in ACN and ~28 ps in MeOH), which is attributed to the TICT process. Theoretical calculations indicate that the benzimidazole group in C7 forms an intramolecular hydrogen bond with the carbonyl oxygen of the benzopyran moiety, stabilizing the molecule's planar structure. In contrast, C30 is unable to form intramolecular hydrogen bonds due to the presence of a methyl group on the nitrogen atom, which increases steric hindrance and reduces molecular stability. This steric hindrance promotes dihedral twisting between the benzimidazole and benzopyran groups in C30, facilitating the TICT process in both ACN and MeOH. Furthermore, a comparison of the τ_2 time constants of C30 in ACN and MeOH reveals that the TICT process in MeOH (28 ps) is substantially prolonged compared to that in ACN (11 ps). This finding is consistent with the study by Ahmed *et al.*, who investigated the TICT process in organic dye molecules, specifically cyanoacrylic dyes, and suggested that hydrogen bonding can prolong the lifetime of the TICT process.[55]

Fluorescence quantum yields

At room temperature and pressure, the fluorescence quantum yields (QYs) of C7 and C30 in ACN and MeOH were measured using a FluoroMax+ spectrofluorometer. The results, summarized in Table 6, show that the QYs for C7 in ACN (87%), C7 in

Table 5 Kinetic parameters of C7 and C30 in ACN and MeOH were obtained by global fitting

Sample	Solvent	τ_1/ps	τ_2/ps	τ_3/ps	τ_4
C7	ACN	0.58 ± 0.01	—	33.54 ± 0.59	~ns
	MeOH	0.85 ± 0.02	—	42.38 ± 1.29	~ns
C30	ACN	0.60 ± 0.01	10.84 ± 1.14	76.07 ± 4.25	~ns
	MeOH	0.48 ± 0.09	28.49 ± 2.87	96.48 ± 18.28	~ns

Table 6 The fluorescence quantum yields (QYs) of C7 and C30 in ACN and MeOH

Sample	Solvent	QY
C7	ACN	87%
	MeOH	97%
C30	ACN	78%
	MeOH	60%

MeOH (97%), C30 in ACN (78%), and C30 in MeOH (60%) exhibit distinct differences. Notably, the QYs for C30 in both solvents are significantly lower than those for C7. This reduction in quantum yield for C30 is attributed to the presence of the TICT process within the C30 molecule, as evidenced by transient absorption spectra and TDDFT calculations. Furthermore, the reduced quantum yield of C30 in MeOH compared to ACN is primarily due to hydrogen bonding between C30 and MeOH molecules, which stabilizes the TICT state and consequently diminishes fluorescence emission efficiency.

Table 7 Bond length information (Å) of C7 and C30 hydrogen-bonded complexes

	C7–ACN		C7–MeOH		C30–ACN		C30–MeOH	
Molecule	S_0	S_1	S_0	S_1	S_0	S_1	S_0	S_1
C_1–O_1	1.222	1.220	1.230	1.228	1.216	1.214	1.225	1.223
N_2–C_3	1.327	1.345	1.330	1.345	1.324	1.345	1.329	1.345
N_1–H_3⋯O_1	2.029	2.016	2.046	2.039	—	—	—	—
C_1–O_1⋯H_1	—	—	1.837	1.808	—	—	1.829	1.802
C_3–N_2⋯H_2	—	—	1.739	1.736	—	—	1.781	1.748

Electrostatic potential and frontier molecular orbitals

ESP analysis is a reliable tool for identifying the regions of hydrogen bond formation between solute and solvent molecules.[15,37] Fig. S3 presents the ESP maps for C7, C30, ACN, and MeOH. Red regions correspond to low ESP, indicating areas of high electronegativity and nucleophilicity, while blue regions represent high ESP, characteristic of low electronegativity and electrophilicity. The C=O and C=N groups in both C7 and C30 are marked by deep red regions, reflecting their strong electron-withdrawing characteristics. Since nitrogen is more electronegative than carbon, nitrogen atoms in these groups exhibit stronger electron-withdrawing capabilities. In C30, the distance between the methyl group's carbon atom and the oxygen atom exceeds 3 Å in both the ground and excited states, preventing intramolecular hydrogen bond formation. Conversely, C7 forms a stable N–H⋯O hydrogen bond. The O–H group in MeOH appears as a deep blue region, reflecting its strong electron-donating capability as a protonic solvent and its role as a hydrogen bond donor. In contrast, the C–H group in ACN is depicted in light blue, indicating weak electron-donating ability. Therefore, both C7 and C30 can form hydrogen bonds in MeOH at two sites: one at the carbonyl oxygen (C–O⋯H) and the other at the nitrogen atom in the benzimidazole group (C–N⋯H).

To further investigate the redistribution of electron density upon excitation to the S_1 state, we performed frontier molecular orbital calculations, as illustrated in Fig. S4. The analysis reveals a transition from the highest occupied molecular orbital (HOMO) to the lowest unoccupied molecular orbital (LUMO), corresponding to the $S_0 \rightarrow S_1$ excitation. As shown, both the HOMO and LUMO of C7 and C30 display distinct π and π^* characteristics, respectively, confirming a $\pi \rightarrow \pi^*$ transition upon excitation to the S_1 state. Notably, following photoexcitation, a significant ICT occurs, with electron density shifting from the benzimidazole moiety to the benzopyranone group in

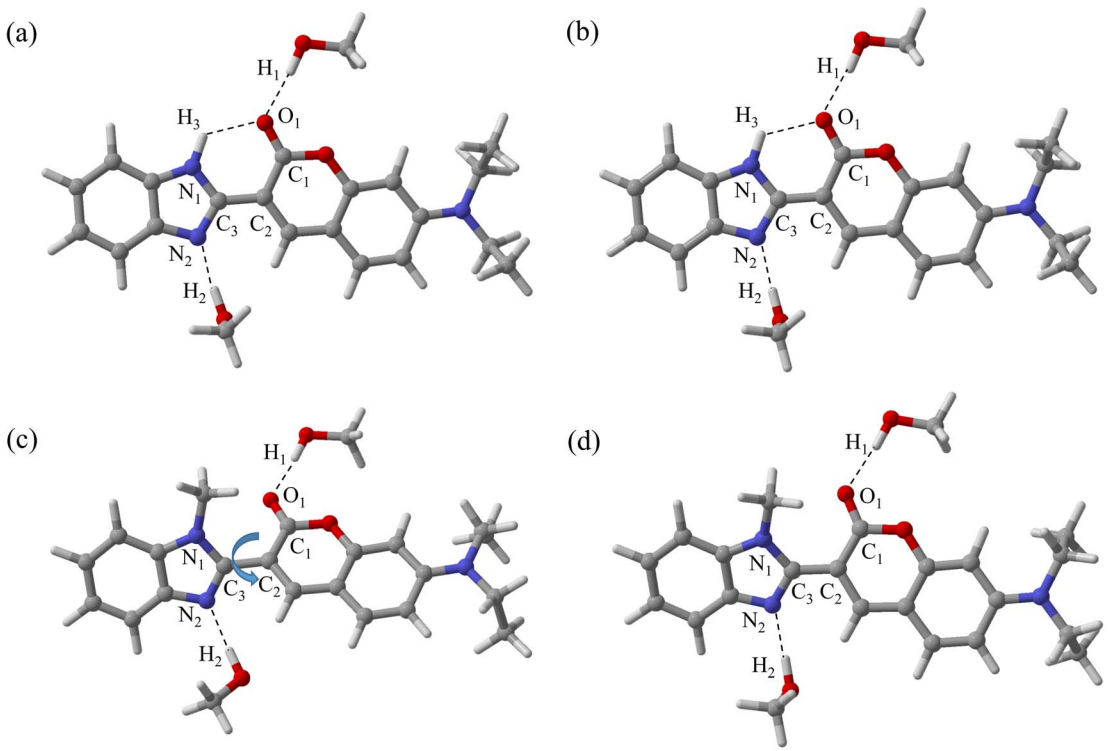

Fig. 6 Geometric configurations of the C7–MeOH/C30–MeOH in S_0 (a and c) and S_1 (b and d).

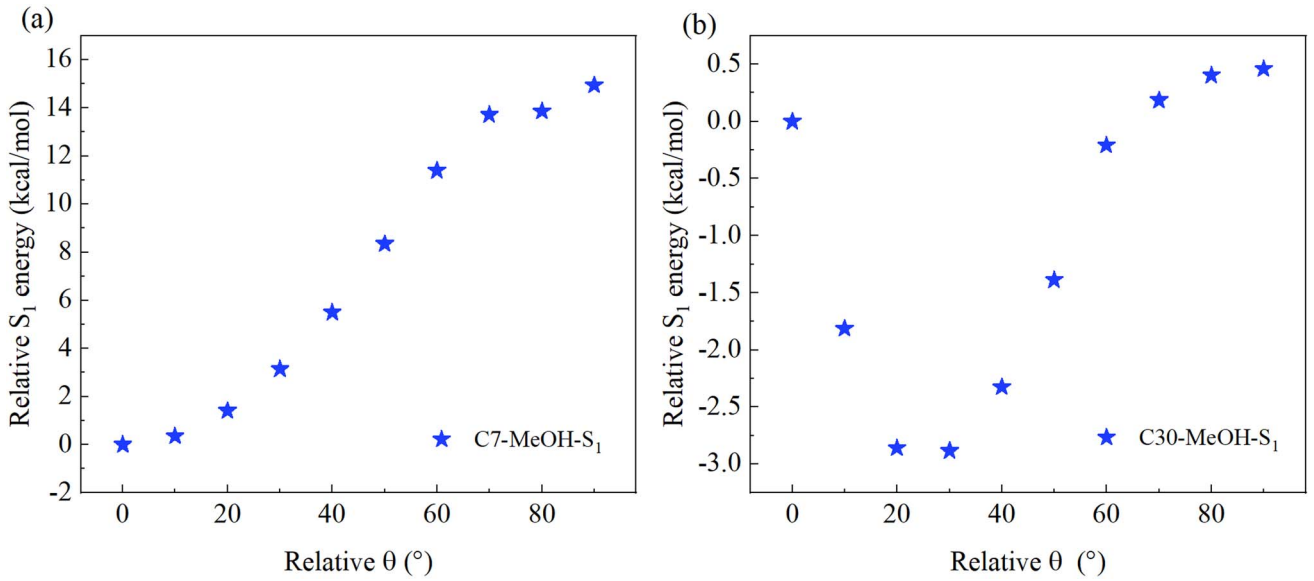

Fig. 7 The potential energy surface of the hydrogen bond complex formed by C7 and C30 in MeOH solvent at S_1 state (relative $\theta = 0°$ refers to the optimized dihedral angle in the ground state).

the hydrogen-bonded complexes of C7 and C30.[30,56] This is accompanied by a pronounced redistribution of charge density, emphasizing strong ICT effects. Additionally, Mulliken charge analysis was conducted on key atoms. For instance, in the C7–MeOH complex, a comparison between the S_0 and S_1 states reveals that the charges on O_1, C_1, and C_2 shift from −0.320, 0.275, and −0.044 C in the ground state to −0.318, 0.264, and −0.091 C in the excited state, representing changes of 0.002, 0.011, and 0.047 C, respectively. These shifts further corroborate the substantial ICT behavior observed.

Optimized geometric configurations

Molecular conformation plays a crucial role in determining the effects of hydrogen bonding on C7 and C30. In combination with ESP analysis, the geometries of C7–MeOH and C30–MeOH hydrogen-bonded complexes were examined, as illustrated in Fig. 6. The key bond lengths for these hydrogen-bonded complexes obtained from the calculations are summarized in Table 7. In the C7–MeOH and C30–MeOH complexes, from the S_0 to S_1 states, the lengths of the intermolecular hydrogen bonds C_1–O_1⋯H_1 and C_3–N_2⋯H_2 both shorten. This contraction suggests a significant increase in hydrogen bond strength, promoting the ICT state. Additionally, the intramolecular hydrogen bond lengths in C7–ACN and C7–MeOH change from 2.029 and 2.046 Å in the ground state to 2.016 and 2.039 Å in the excited state, respectively, indicating a slight increase in hydrogen bond strength. As shown in Table S4, the hydrogen bond binding energies of C7 and C30 in ACN and MeOH have both increased from the S_0 state to the S_1 state, indicating that the excited state is more conducive to hydrogen bond formation and thereby favoring intramolecular charge transfer. As depicted in Fig. 6, the dihedral angle N_1–C_3–C_2–C_1 in C7–MeOH shifts slightly from 0.09° in the S_0 state to 0.11° in the S_1 state, while in C30–MeOH, the dihedral angle N_1–C_3–C_2–C_1 decreases significantly from −46.95° in the S_0 state to −29.42° in the S_1 state, corresponding to a torsion of 17.53°. Meanwhile, according to theoretical calculations, during this dihedral torsion, the emission peak of S_1 state redshifts from 458 nm to 494 nm, further supporting the occurrence of the TICT process in C30, as observed in the TA spectra, indicates that C7–MeOH has undergone the TICT process.

In order to analyze in detail the influence of MeOH on the excited-state dynamics of C7 and C30, the potential energy surfaces of the two molecules were calculated using the CAM-B3LYP/Def2SVP functional and basis set combined with the SMD solvent model, As shown in Fig. 7, the horizontal coordinate represents the relative dihedral angles (N_1–C_3–C_2–C_1) of the C30–MeOH hydrogen bond complex, and the vertical coordinate represents the relative energy of the hydrogen bond complex in the S_1 state. As shown in Fig. 7, the relative energy of the C30–MeOH complex in the S_1 state gradually decreases by 2.88 kcal mol^{-1} without encountering an energy barrier as the relative dihedral angle increases from 0° to 30°. In C7–MeOH, with the torsion of the relative dihedral angle, the relative energy of the S_1 state gradually increases up to 15.12 kcal mol^{-1}. Through the comparison of the potential energy surfaces of these two complexes, it is further indicated that the structural characteristics of the C7–MeOH complex are conducive to the formation of stable intramolecular hydrogen bonds, the planar configuration of the benzimidazole and benzopyran parts was stabilized, effectively inhibiting the TICT process.

Conclusions

In conclusion, we investigated the excited-state dynamics of C7 and C30 in highly polar aprotic (ACN) and protic (MeOH) solvents using a combination of steady-state and fs-TA spectroscopy, complemented by TDDFT calculations. Our findings

reveal that both intramolecular and intermolecular hydrogen bonding are pivotal in the excited-state dynamics, providing novel insights into the dynamics of the TICT process. Steady-state spectral analysis demonstrated that there is a strong linear correlation between absorption, fluorescence emission and Stokes shift and solvent parameters, and these parameters have a significant impact on the observed shift. Fs-TA spectroscopy provided a detailed temporal resolution of the excited-state dynamics, distinguishing various processes such as ICT, TICT, solvation, and fluorescence emission. The structural characteristics of C7 complexes facilitate the formation of stable intramolecular hydrogen bonds in polar solvents, thereby stabilizing the planar configuration of the benzimidazole and benzopyran moieties and effectively suppressing the TICT process. In contrast, compound C30 complexes, which lack the capacity to form intramolecular hydrogen bonds and are subject to steric hindrance from the methyl group attached to the nitrogen atom, exhibit greater flexibility in their dihedral angle, promoting the TICT process. Quantum chemical calculations confirmed the presence of intramolecular hydrogen bonding in C7 in both ACN and MeOH, further substantiating its structural stability. Overall, this study elucidates the photochemical and photophysical behavior of C7 and C30 in different solvent environments, providing critical insights for the molecular design of fluorescent dyes. The findings underscore the pivotal role of hydrogen bonding in controlling excited-state dynamics in polar solvents, laying an important theoretical foundation for the optimization of luminescent properties in fluorescent materials.

Author contributions

Jing Ge: writing – original draft, investigation, methodology, conceptualization, funding acquisition. Jing Xiao: writing – original draft, methodology, investigation. Bingqian Xue: investigation, writing – review & editing. Duidui Liu: investigation, writing – review & editing. Bingqi Du: investigation. Xilin Bai: writing – review & editing, conceptualization, funding acquisition, investigation, supervision, writing – original draft.

Conflicts of interest

The authors declare that they have no known competing financial interests or personal relationships that could have appeared to influence the work reported in this paper.

Data availability

All data supporting the findings of this study are included within the article and SI. As all experimental data, results, and analyses have been fully incorporated into the manuscript, there are no additional datasets stored elsewhere that would require external access provisions.

The supplementary information encompasses essential data such as geometric configurations, potential energy surfaces, electrostatic potentials, along with K–T and experience model parameters tailored for various solvents. It also details bond lengths, bond binding energies, and a full set of calculated *XYZ* coordinates. See DOI: **https://doi.org/10.1039/d5ra02669e**.

Acknowledgements

This work was supported by the National Natural Science Foundation of China (NSFC) (No. 21903050) and Research Project Supported by Shanxi Scholarship Council of China Scientific (No. 2021-092).

References

1 K. Hanaoka, S. Iwaki, K. Yagi, T. Myochin, T. Ikeno, H. Ohno, E. Sasaki, T. Komatsu, T. Ueno, M. Uchigashima, T. Mikuni, K. Tainaka, S. Tahara, S. Takeuchi, T. Tahara, M. Uchiyama, T. Nagano and Y. Urano, *J. Am. Chem. Soc.*, 2022, **144**, 19778–19790.
2 G. J. Zhao and K. L. Han, *Phys. Chem. Chem. Phys.*, 2010, **12**, 8914–8918.
3 H. Zhang, D. C. Zeitz and J. Z. Zhang, *J. Phys. Chem. Lett.*, 2023, **14**, 8095–8099.
4 R. K. Venkatraman and A. J. Orr Ewing, *J. Am. Chem. Soc.*, 2019, **141**, 15222–15229.
5 C. Wang, Q. L. Qiao, W. J. Chi, J. Chen, W. J. Liu, D. Tan, S. McKechnie, D. Lyu, X. F. Jiang, W. Zhou, N. Xu, Q. S. Zhang, Z. C. Xu and X. G. Liu, *Angew. Chem., Int. Ed.*, 2020, **59**, 10160–10172.
6 W. j. Chi, Q. l. Qiao, R. Lee, W. j. Liu, Y. S. Teo, D. Gu, M. J. Lang, Y. T. Chang, Z. c. Xu and X. g. Liu, *Angew. Chem., Int. Ed.*, 2019, **58**, 7073–7077.
7 P. A. Rose, *J. Phys. Chem. Lett.*, 2023, **14**, 10849–10855.
8 X. M. Niu, Z. R. Kuang, M. Planells, Y. Y. Guo, N. Robertson and A. D. Xia, *Phys. Chem. Chem. Phys.*, 2020, **22**, 15743–15750.
9 P. Dahiya, M. Kumbhakar, T. Mukherjee and H. Pal, *Chem. Phys. Lett.*, 2005, **414**, 148–154.
10 K. Rotkiewicz, K. H. Grellmann and Z. R. Grabowski, *Chem. Phys. Lett.*, 1973, **19**, 315–318.
11 G. Y. Gao, W. J. Qu, B. B. Shi, Q. Lin, H. Yao, J. Chang and Y. Cai, *Sens. Actuators, B*, 2015, **213**, 501–507.
12 L. M. Loftus, E. C. Olson, D. J. Stewart, A. T. Phillips, K. Arumugam, T. M. Cooper, J. E. Haley and T. A. Grusenmeyer, *Inorg. Chem.*, 2021, **60**, 16570–16583.
13 J. Ge, Q. Zhang, J. Jiang, Z. G. Geng, S. L. Jiang, K. L. Fan, Z. K. Guo, J. H. Hu, Z. W. Chen, Y. Chen, X. P. Wang and Y. Luo, *Phys. Chem. Chem. Phys.*, 2015, **17**, 13129–13136.
14 X. F. Zhou, F. Y. Su, H. G. Lu, P. Senechal-Willis, Y. Q. Tian, R. H. Johnson and D. R. Meldrum, *Biomaterials*, 2012, **33**, 171–180.
15 J. Ge, X. D. Zhang, Y. Peng and X. L. Bai, *RSC Adv.*, 2023, **13**, 4924–4931.
16 M. Iwamura, A. Fukui, K. Nozaki, H. Kuramochi, S. Takeuchi and T. Tahara, *Angew. Chem., Int. Ed.*, 2020, **59**, 23154–23161.
17 F. Z. Ling, D. J. Liu, S. Li, W. Li and P. F. Wang, *J. Chem. Phys.*, 2019, **151**, 094302.

18 X. M. Wu, X. R. Sun, Z. Q. Guo, J. B. Tang, Y. Q. Shen, T. D. James, H. Tian and W. H. Zhu, *J. Am. Chem. Soc.*, 2014, **136**, 3579–3588.
19 M. Maniyazagan, R. Mariadasse, M. Nachiappan, J. Jeyakanthan, N. Lokanath, S. Naveen, G. Sivaraman, P. Muthuraja, P. Manisankar and T. Stalin, *Sens. Actuators, B*, 2018, **254**, 795–804.
20 H. Li, J. H. Han, H. F. Zhao, X. C. Liu, L. Ma, C. F. Sun, H. Yin and Y. Shi, *J. Cluster Sci.*, 2018, **29**, 585–592.
21 Y. Li, C. F. Sun, J. H. Han, Q. Zhou, B. F. Cao, H. Yin and Y. Shi, *J. Lumin.*, 2020, **221**, 117110.
22 A. Das, S. Das, A. Biswas and N. Chattopadhyay, *J. Phys. Chem. B*, 2021, **125**, 13482–13493.
23 H. Li, H. Yin, X. C. Liu, Y. Shi, M. X. Jin and D. J. Ding, *Spectrochim. Acta, Part A*, 2017, **184**, 270–276.
24 G. Li, D. Magana and R. B. Dyer, *J. Phys. Chem. B*, 2012, **116**, 12590–12596.
25 W. Zhang, J. Kong, D. H. Hu, M. Tao, X. M. Niu, S. Vdović, D. Aumiler, Y. G. Ma and A. D. Xia, *J. Phys. Chem. C*, 2020, **124**, 5574–5582.
26 W. Zhang, W. Q. Xu, G. X. Zhang, J. Kong, X. M. Niu, J. M. Chan, W. M. Liu and A. D. Xia, *J. Phys. Chem. B*, 2021, **125**, 4456–4464.
27 Z. R. Kuang, Q. J. Guo, X. Wang, H. W. Song, M. Maroncelli and A. Xia, *J. Phys. Chem. Lett.*, 2018, **9**, 4174–4181.
28 J. Kong, W. Zhang, G. Li, D. Huo, Y. Y. Guo, X. M. Niu, Y. Wan, B. Tang and A. D. Xia, *J. Phys. Chem. Lett.*, 2020, **11**, 10329–10339.
29 M. V. Nikolaeva and M. V. Puzyk, *Opt. Spectrosc.*, 2017, **122**, 625–627.
30 A. K. Satpati, M. Kumbhakar, S. Nath and H. Pal, *Photochem. Photobiol.*, 2009, **85**, 119–129.
31 N. Weiß, C. H. Schmidt, G. Thielemann, E. Heid, C. Schröder and S. Spange, *Phys. Chem. Chem. Phys.*, 2021, **23**, 1616–1626.
32 J. M. Xu, J. S. Chen, S. L. Dong, A. P. Fu, H. L. Li and T. S. Chu, *J. Phys. Org. Chem.*, 2016, **29**, 305–311.
33 Z. C. Xu, X. G. Liu, Q. L. Qiao and N. Xu, *Acta Chim. Sin.*, 2022, **80**, 553–562.
34 C. Chudoba, E. T. J. Nibbering and T. Elsaesser, *J. Phys. Chem. A*, 1999, **103**, 5625–5628.
35 S. Senthilkumar, S. Nath and H. Pal, *Photochem. Photobiol.*, 2007, **80**, 104–111.
36 N. Barman, D. Singha and K. Sahu, *J. Phys. Chem. A*, 2013, **117**, 3945–3953.
37 J. Ge, X. D. Zhang, Z. B. Li, B. Q. Xue and X. L. Bai, *RSC Adv.*, 2023, **13**, 21746–21753.
38 W. Humphrey, A. Dalke and K. Schulten, *J. Mol. Graphics*, 1996, **14**, 33–38.
39 M. J. Frisch, G. W. Trucks, H. B. Schlegel, G. E. Scuseria, M. A. Robb, J. R. Cheeseman, G. Scalmani, V. Barone, B. Mennucci and G. A. Petersson, *Gaussian 09, Revision D. 01*, Gaussian, Inc., Wallingford CT, USA, 2009, vol. 620.
40 M. J. Kamlet, J. L. M. Abboud, M. H. Abraham and R. Taft, *J. Org. Chem.*, 1983, **48**, 2877–2887.
41 B. Maity, A. Chatterjee and D. Seth, *Photochem. Photobiol.*, 2014, **90**, 734–746.
42 J. Catalán, *J. Phys. Chem. B*, 2009, **113**, 5951–5960.
43 M. H. Queiroz, T. V. Alves, R. Rivelino and S. Canuto, *ACS Omega*, 2024, **9**, 22102–22111.
44 S. K. Behera, A. Karak and G. Krishnamoorthy, *J. Phys. Chem. B*, 2015, **119**, 2330–2344.
45 J. Zhao, L. Fan, L. Feng, B. Jin and S. Zhao, *J. Phys. Org. Chem.*, 2022, **36**, e440.
46 B. U. Emenike, A. Sevimler, A. Farshadmand and A. J. Roman, *Phys. Chem. Chem. Phys.*, 2023, **25**, 17808–17814.
47 B. Taheri, M. S. Zakerhamidi, A. N. Shamkhali, R. Kian and A. A. Sadeghan, *Sci. Rep.*, 2025, **15**, 15716.
48 M. J. Kamlet, J. L. Abboud and R. W. Taft, *J. Am. Chem. Soc.*, 1977, **99**, 6027–6038.
49 X. G. Liu, J. M. Cole and K. S. Low, *J. Phys. Chem. C*, 2013, **117**, 14731–14741.
50 H. Sotome, T. Nagasaka, K. Une, S. Morikawa, T. Katayama, S. Kobatake, M. Irie and H. Miyasaka, *J. Am. Chem. Soc.*, 2017, **139**, 17159–17167.
51 M. L. Shelby, P. J. Lestrange, N. E. Jackson, K. Haldrup, M. W. Mara, A. B. Stickrath, D. Zhu, H. Lemke, M. Chollet and B. M. Hoffman, *J. Am. Chem. Soc.*, 2016, **138**, 8752–8764.
52 H. Mandal, J. L. Rao, J. i. Kulhánek, F. Bureš and P. R. Bangal, *J. Phys. Chem. C*, 2023, **127**, 4724–4740.
53 L. Cong, H. Yin, Y. Shi, M. X. Jin and D. J. Ding, *RSC Adv.*, 2015, **5**, 1205–1212.
54 J. Ge, B. Q. Xue, Z. B. Li, J. Xiao and X. L. Bai, *Chin. J. Lumin.*, 2024, **45**, 671–680.
55 A. M. El-Zohry, E. A. Orabi, M. Karlsson and B. Zietz, *J. Phys. Chem. A*, 2021, **125**, 2885–2894.
56 R. Ghosh and B. Manna, *Phys. Chem. Chem. Phys.*, 2017, **19**, 23078–23084.